Determination of grounding line on the Amery Ice Shelf using Sentinel-1 radar interferometry data

LEI Haobo, ZHOU Chunxia* & CHEN Yiming

Chinese Antarctic Center of Surveying and Mapping, Wuhan University, Wuhan 430079, China

Abstract   Delineation of the grounding line (GL) is necessary for calculating the mass balance of Antarctica, but GL measurements for most of the continent remain at a relatively coarse level. We used Sentinel-1 constellation data to map the GL of the Amery Ice Shelf (AIS) using double-differential synthetic aperture radar interferometry. The ice thickness anomaly deduced from hydrostatic equilibrium and existing Antarctic GL products is compared with our result. With this new and very accurate GL, we detected new ice rises in the north of the AIS. Our new measurement shows no major change of the AIS GL, particularly in the southernmost part.

1   Introduction

The Antarctic ice sheet holds 26.5 million km^3 of ice, and a small mass imbalance in this can make a major contribution to sea level rise (Rignot et al., 2013; Rignot and Thomas, 2002). Long-term monitoring of Antarctic mass balance is essential in global climate change research. The grounding line (GL) is the boundary line between the inland grounded ice sheet and floating ice shelf, and its location is sensitive to ice thickness, sea level, and ocean temperature. The GL location greatly influences the stability of marine ice sheets (Weertman, 1974), and is important for ice sheets, ice shelves, and oceanographic modeling. The Amery Ice Shelf (AIS) is the largest ice shelf in East Antarctica, accounting for 16% of the total mass of the East Antarctic ice sheet (Fricker et al., 2000). Continuous observation of the AIS GL over long periods is crucial for understanding mass balance changes in East Antarctica.

The grounding zone (Figure 1) is a crucial region

extending over a few kilometers, where a grounded ice sheet evolves into a freely floating ice shelf (Brunt et al., 2010). In Figure 1, F is the landward limit of ice flexure from tidal movement and G is the true GL, which can be detected by synthetic aperture radar interferometry (InSAR), I_b is the point of break in slope, I_m is the local minimum in topography, and H marks the end of the flexure zone (Fricker et al., 2009).

Remote sensing techniques are widely used to map the GL. The MODIS-based Mosaic of Antarctica (MOA) and Landsat 7 Image Mosaic of Antarctica (LIMA) are used to generate GL products for the entire Antarctic (Bindschadler et al., 2007; Scambos et al., 2007). In the double-differential synthetic aperture radar interferometry (DDInSAR) method, ERS-1/2, RADARSAT-1/2, and ALOS-1 have been used to extract the first high-precision GLs around Antarctica from 1994 to 2009 (Rignot et al., 2011). Studies have used radio echo sounding (RES), ERS-1/2, MODIS, and ICESat data to map the GL on the AIS (Fricker et al., 2009, 2002; Wang et al., 2002). The combination of Landsat 8 Operational
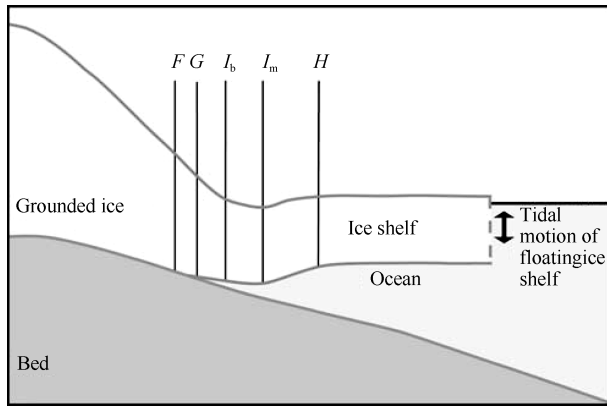
Figure 1 Features of grounding zone (Fricker et al., 2009).

Land Imager (OLI) and ICESat data has been used to produce a new adjusted GL of the AIS (Xie et al., 2016). Compared with other methods, DDInSAR has demonstrated successful application to GL mapping. The accuracy of this method is reported to be better than 100 m in the horizontal direction (Rignot et al., 2011).

Before 2014, GL mapping was limited by the few synthetic aperture radar (SAR) missions offering short-term, repeat-pass data. GL mapping has the essential capability to map the differential vertical displacement of floating ice at tidal frequency in areas where ice moves rapidly (Scheuchl et al., 2016). Launched in April 2014 and April 2015 respectively, Sentinel-1A and Sentinel-1B are both C-band SAR satellites. A single satellite features a 12-day repeat cycle, and the repeat cycle of the constellation is six days. Sentinel-1 is designed to address primarily medium-to-high resolution applications using an Interferometric Wide Swath (IW) mode of operation that features both a wide swath (250 km) and high spatial resolution (5 m × 20 m) (Torres et al., 2012). The IW mode of Sentinel-1 is implemented using terrain observation by progressive scans (TOPS) mode (Prats-Iraola et al., 2015), which poses challenges in interferometric phase analysis.

Sentinel-1A data have been used to monitor the rapid GL retreat of the Pope, Smith, and Kohler glaciers in West Antarctica (Scheuchl et al., 2016). Over the past decade, few SAR data have been used to observe the GL of the AIS, and the accuracy of past monitoring requires verification. In the present study, we used Sentinel-1 constellation data to map the AIS GL using DDInSAR. First, we introduce our data and study area. We then describe the Sentinel-1 data processing method and hydrostatic equilibrium (HE) theory, which is used to the calculate ice thickness anomaly for comparison. Finally, the quality of the AIS GL is assessed against existing GL products, and changes of GL position are investigated.

2　Study area and data

2.1　AIS

AIS, the third largest ice shelf in Antarctica (Figure 2),

drains the grounded portion of the Lambert Glacier–AIS system (Wen et al., 2010). The ice flows toward the coast in a convergent pattern so that it focuses on the front of the AIS, which accounts for only 2% of the total East Antarctic coastline. Continuous observation of the GL over long periods in this area is crucial to understand dynamic changes in East Antarctica.
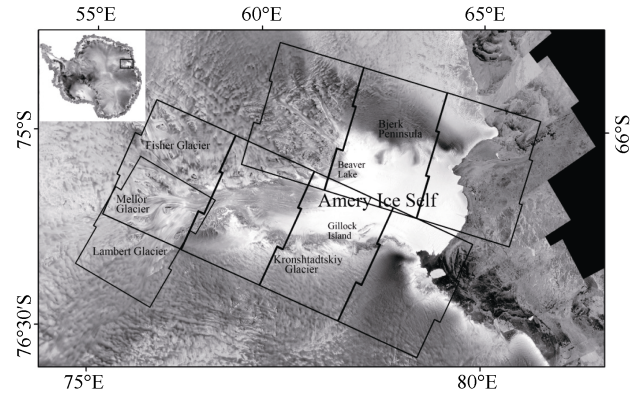
Figure 2 Radarsat image mosaic of AIS in East Antarctica (black polygons are areas of Sentinel-1 IW acquisitions).

2.2　Sentinel data

The SAR instrument aboard Sentinel-1 supports four modes with variable resolution and coverage, i.e., IW Swath, Extra-Wide Swath (EW), Stripmap (SM), and Wave (WV). IW and EW modes provide large swath widths of 250 km (three sub-swaths) and 400 km (five sub-swaths) at ground resolutions 5 m × 20 m and 20 m × 40 m, respectively (Yagüe-Martínez et al., 2016). Sentinel-1 IW mode uses three sub-swaths in IW mode (IW1, IW2, and IW3), and small overlaps are noted between bursts and sub-swaths. In contrast with ScanSAR mode, the TOPS SAR acquisition mode eliminates scalloping and azimuth ambiguities. Given the particularity of TOPS mode, the process of interferometry is different from that of Stripmap (Prats-Iraola et al., 2015). High azimuth co-registration accuracy must be guaranteed to maintain effective signal coherence; the value should be 1 cm for Sentinel-1, which corresponds to approximately 1/1000 azimuth resolution cells (De Zan et al., 2014). In our study, a spectral diversity method that considers the interferometric phase of the burst overlap region was used to improve co-registration refinement (Wegmüller et al., 2015; Scheiber and Moreira, 2000).

Sentinel-1 data are applicable to detecting GLs in Antarctica with a short cycle and large swath widths. To map the AIS GL, 27 Sentinel-1 IW acquisitions were used to create nine double-differential SAR interferograms (DDSIs) (Table 1). Figure 2 illustrates the ranges of Sentinel-1 IW acquisitions. For selecting suitable data, the CATS2008a tide model (Hall, 2006) was used to estimate ocean tidal amplitude.

Table 1   Parameters of Sentinel-1 IW pairs. B_{perp} is perpendicular baseline, H_{tide} is tide height predicted by CATS2008a tide model, and ΔH_{tide} is the difference in tide heights

Platform	DDSI	Orbit	Slice number	Date	B_{perp}/m	H_{tide}/m	ΔH_{tide} /m
Sentinel-1B		2829	4	20161105	45.43	0.15	
Sentinel-1A	DDSI-1	13900	4	20161111	8.35	−0.24	0.87
Sentinel-1B		3004	4	20161117		0.24	
Sentinel-1B		2829	5	20161105	43.16	0.16	
Sentinel-1A	DDSI-2	13900	5	20161111	7.65	−0.28	1.03
Sentinel-1B		3004	5	20161117		0.31	
Sentinel-1A		13550	6	20161018	88.26	0.33	
Sentinel-1B	DDSI-3	2654	6	20161024	151.10	−0.23	0.83
Sentinel-1A		13725	6	20161030		0.04	
Sentinel-1B		2829	7	20161105	39.55	0.15	
Sentinel-1A	DDSI-4	13900	7	20161111	6.25	−0.30	1.10
Sentinel-1B		3004	7	20161117		0.35	
Sentinel-1A		13506	8	20161015	147.04	0.08	
Sentinel-1B	DDSI-5	2610	8	20161021		0.12	−0.69
Sentinel-1B		2785	8	20161102	91.57	0.35	
Sentinel-1A		13856	8	20161108		−0.30	
Sentinel-1A		11217	2	20160511	158.04	0.24	
Sentinel-1A	DDSI-6	11567	2	20160604	32.97	−0.07	0.24
Sentinel-1A		11917	2	20160628		−0.14	
Sentinel-1A		11217	1	20160511	156.75	0.20	
Sentinel-1A	DDSI-7	11567	1	20160604	124.50	−0.05	0.18
Sentinel-1A		11917	1	20160628		−0.12	
Sentinel-1A		11217	3	20160511	159.06	0.24	
Sentinel-1A	DDSI-8	11567	3	20160604	125.50	0.03	−0.09
Sentinel-1A		11917	3	20160628		−0.27	
Sentinel-1A	DDSI-9	13550	5	20161018	88.86	0.28	
Sentinel-1B		2654	5	20161024		−0.18	0.02
Sentinel-1B		2829	5	20161105	43.16	0.16	
Sentinel-1A		13900	5	20161111		−0.28	

2.3 RES data

RES data measured by Russians and Australians were used to obtain the AIS ice thickness over the past 50 years. We compared aerial RES ice thickness results of the AIS from 1987 to 2003 collected by the Australian National Antarctic Research Expedition (ANARE) and Russian Antarctic Expedition with the ice thickness anomaly deduced from HE theory. RES ice thickness precision is better than 70 m and terrain precision better than 20 m (Allison and Hyland, 2010).

3 Methods

3.1 GL mapping from sentinel-1

As InSAR are used to map the GL, the interferometric phase ϕ is composed of the reference phase ϕ_{ref},

topographic phase ϕ_{topo}, deformation phase ϕ_{def}, orbit errors ϕ_{orb}, and atmospheric delays ϕ_{atm}. Given that the Sentinel-1 orbits are well known and assuming that atmospheric delays are negligible, the interferometric phase is given by

$$\phi = \phi_{ref} + \phi_{topo} + \phi_{def} . \qquad (1)$$

As surface topography is removed using an external DEM, the remaining differential InSAR signals of floating ice represent surface displacement ϕ_{def} as the summation of horizontal ice flow ϕ_{flow} and vertical tidal deflection ϕ_{tide}. We assume that the ice flow is steady over the observation periods. Tide-only interferograms are formed by calculating the difference between two interferograms, which span the same time interval between data acquisitions (Rignot, 1998). The phase of the double-differential SAR interferogram $\Delta\phi_{double}$ is given by

$$\Delta\phi_{\text{double}} = \phi_{\text{tide-1}} - \phi_{\text{tide-2}}. \tag{2}$$

In DDSIs, the inland grounded ice sheet is tide-free, and the freely floating ice shelf moves vertically because of tidal forcing. The grounding zone exhibits vertical displacement over a few kilometers to bring ice into HE, and the GL can be detected by interpreting the inner land limit of dense fringes.

An accuracy of 1/1000 of a pixel in the azimuth direction is required for TOPS interferometry co-registration. Therefore, the traditional method of estimating the offset of two images by calculating the local spatial correlation function for several small areas is inapplicable. To assure high co-registration accuracy, GAMMA software uses a method considering the effects of scene topography (Werner et al., 2001). The method is based on a lookup table, which features the same size of reference image and contains the coordinate of the corresponding pixel in the other image at each location.

After the co-registration based on a lookup table, we processed all Sentinel-1 data to generate interferograms. The Bamber DEM (Bamber et al., 2008) was used to remove surface topography. Obtaining effective signal coherence for the AIS is challenging due to the ice motion. We selected image pairs with a short cycle to minimize the effect of long-term surface motion and retain the highest coherence levels. The GL cannot be detected if point G (Figure 1) is in a region with rapid ice velocity changes.

After flattening and phase unwrapping, residual sub-fringe phase jumps are observed at the burst edges. This is mainly caused by ice motion. To enhance understanding of this, the total interferometric phase related to ice motion $\Delta\phi_{\text{motion}}$ is given by

$$\phi_{\text{motion}} = -\frac{4\pi}{\lambda} \boldsymbol{v}_{\text{flow}} \cdot \boldsymbol{e}_{\text{LOS}}, \tag{3}$$

where $\boldsymbol{e}_{\text{LOS}}$ is the line of sight (LOS) vector, which varies in the azimuth dimension in the TOPS case because of the steering of antenna pointing within the burst (De Zan et al., 2014). $\boldsymbol{v}_{\text{flow}}$ is the motion vector of the ice and λ is the wavelength. Because the LOS vectors have opposite azimuth directions in adjacent bursts, motion phase in the overlap area can differ from burst to burst. With the existence of phase jumps, generating a high-precision DEM is difficult. Fortunately, residual phase jumps do not affect GL mapping.

3.2 HE theory

The assumption of HE theory allows calculation of ice thickness from the freeboard, which can be determined from the surface DEM:

$$H_{\text{thickness}} = \left[\left(h_{\text{free}} - h_{\text{firn}} \right) \frac{\rho_{\text{seawater}}}{\rho_{\text{seawater}} - \rho_{\text{ice}}} \right] + h_{\text{firn}}, \tag{4}$$

where $H_{\text{thickness}}$ is ice thickness, h_{free} is freeboard height, h_{firn} is the air content of the firn layer expressed in meters

of ice equivalent, ρ_{seawater} is the density of sea water, and ρ_{ice} is ice density. The densities of seawater and ice used here are 1027 and 917 kg·m^{-3}, respectively (Fricker et al., 2001). The firn height was taken from a firn densification model (FDM) and resampled to 1-km grid spacing (Ligtenberg et al., 2014). The freeboard height was calculated by subtracting the EIGEN-64C Geoid (Förste et al., 2013) from the Bamber DEM.

The HE assumption is only valid if the ice shelf is freely floating (Griggs and Bamber, 2011). If the ice shelf is grounded, ice thickness will be grossly overestimated. In the present study, the value of ice thickness difference (ΔT) was calculated by subtracting ice thickness calculated by HE from the RES ice thickness. If that value is close to zero, the ice is floating, otherwise it is grounded. The approximate location of the GL is detected via this method.

To test the accuracy of the ice thickness calculated from HE for the freely floating ice shelf, we estimated uncertainties within the gray polygon of Figure 3a, where the ice is definitely floating; the black line is the synthesized GL and ice shelf mask for Antarctica (Depoorter et al., 2013b). The resulting HE ice thickness has a mean error of −27.86 m and standard deviation of 60.53 m compared with the RES ice thickness (Figure 3b). The error of HE ice thickness is > 100 m in the northwestern AIS, which was caused by marine ice accreting to the base of the ice shelf (Fricker et al., 2001). These large differences were caused by RES echoes reflecting off the marine/meteoric ice interface as opposed to the ice/ocean interface, a result of the increase in salinity and density of the marine ice (Chuter and Bamber, 2015). Figure 3c shows the ice thickness difference profile along the thick green line in Figure 3a. The thickness difference is near zero, indicating that the ice is floating. If the ice is grounded, the ice thickness anomaly would show a rapid increase. Considering that RES data have a thickness accuracy of 75 m, the threshold used to estimate the ice thickness anomaly area is the mean error minus three times the standard deviation (–209.45 m). Figure 3a shows regions where ΔT is < –209.45 m as red dots, indicating that the ice is grounded. This result was used to test the accuracy of the Sentinel-1 GL measurement.

4   Results and discussion

4.1   GL mapping by Sentinel-1 SAR data

To map the Sentinel-1 GL over the AIS (Figure 4), 27 acquisitions were used to generate nine DDSIs (Table 1). Residual sub-fringe phase jumps were observed at the burst edges. The repeat cycle for DDSI-1 to DDSI-5 and DDSI-9 is 6 d with the constellation data of Sentinel-1A and Sentinel-1B. The repeat cycle from DDSI-6 to DDSI-8 is 24 d because of a lack of suitable data, and the coherence of
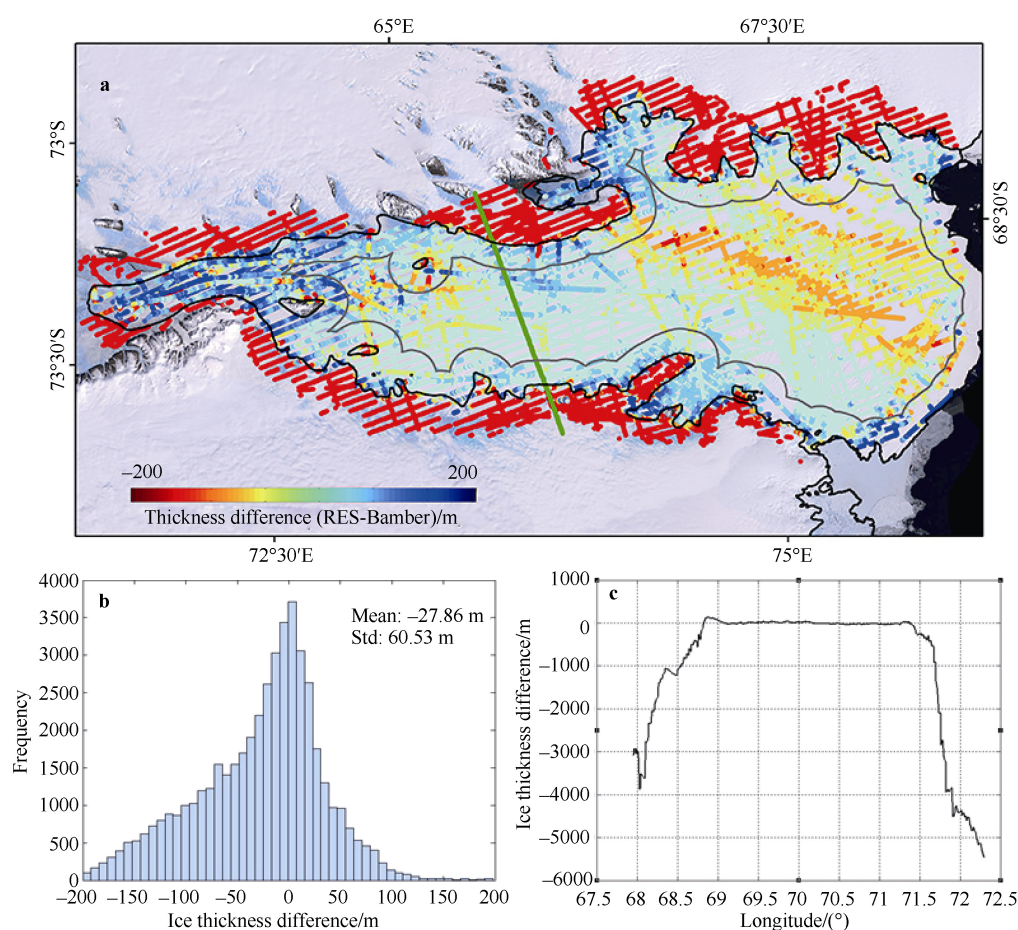
Figure 3   Ice thickness difference between RES data and HE results for AIS (**a**); histogram of ice thickness difference within gray polygon (**b**). Ice thickness difference profile along thick green line in **a** and **c**.

these pairs is relatively low because of surface melt, snowfall, and fast ice flow. We mapped 1809.7 km of the GL, or 91.59% of the AIS, which is easily the most relatively complete InSAR-based GL in the area. Two small ice rises in the Bjerk Peninsula were detected via our measurement (Figures 4b and 4c). Ice rises are important in buttressing local ice shelves (Lenaerts et al., 2014). Prior InSAR GL failed to detect these ice rises because of a lack of SAR pairs in the area. Detecting ice rises of this size is also difficult for optical imagery or altimetry. The regions in Figures 4d, 4e, and 4f differ from previous GLs and are discussed in the following subsection.

4.2   Error analysis

We compared the Sentinel-1 GL with the MOA-derived GL (Scambos et al., 2007), MEaSUREs GL (Rignot et al., 2011), and synthesized GL (Depoorter et al., 2013b). We used the near tool in ArcGIS to calculate the distance between the Sentinel-1 GL and these products. Figure 5 shows histograms of distance. Sentinel-1 and MEaSUREs GLs show strong agreement, because the same method is used. The average distance between Sentinel-1 and

MEaSUREs GLs is 968 m, and the standard deviation is 1264 m. Sentinel-1 and MOA GLs show the largest difference; the mean distance and standard deviation are 1733 and 1874 m, respectively.

We created 1, 2, and 3 km buffers for the Sentinel-1 GL and calculated the percentage of the other GLs falling within those buffers. Table 2 indicates excellent agreement between Sentinel-1 and MEaSUREs GLs. A total of 92.24% of MEaSUREs GLs are within the 3-km buffer, and 72.42% within the 1-km buffer. For the synthesized GLs that use a mix of Antarctic Surface Accumulation and Ice Discharge (Bindschadler et al., 2011), MOA, ICESat, and InSAR GLs, 90.35% lie within the 3-km buffer, and 69.32% within the 1-km buffer. The MOA GL, which extracts the point I_b, differs more from the Sentinel-1 GL; 79.32% of the MOA GL lies within the 3-km buffer and 52.06% within the 1-km buffer. Different methods extract distinct points, and the GL location is not defined explicitly. The line retreats and advances as tides change. Therefore, assessing the GL quality and analyzing changes is a complex issue. In our study, HE results were used to analyze GL changes of the AIS.
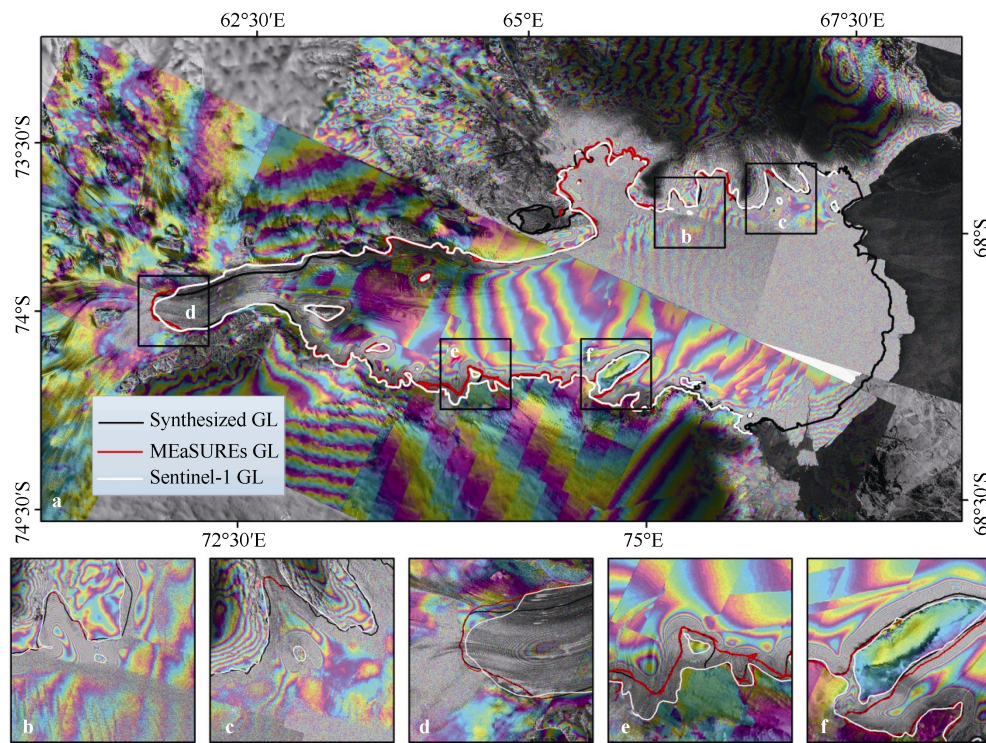
Figure 4　GL of AIS mapped by Sentinel-1(**a**); **b** and **c** are insets of two ice rises on Bjerk Peninsula; **d** is southernmost GL of AIS; **e** and **f** insets show details of eastern side of AIS.
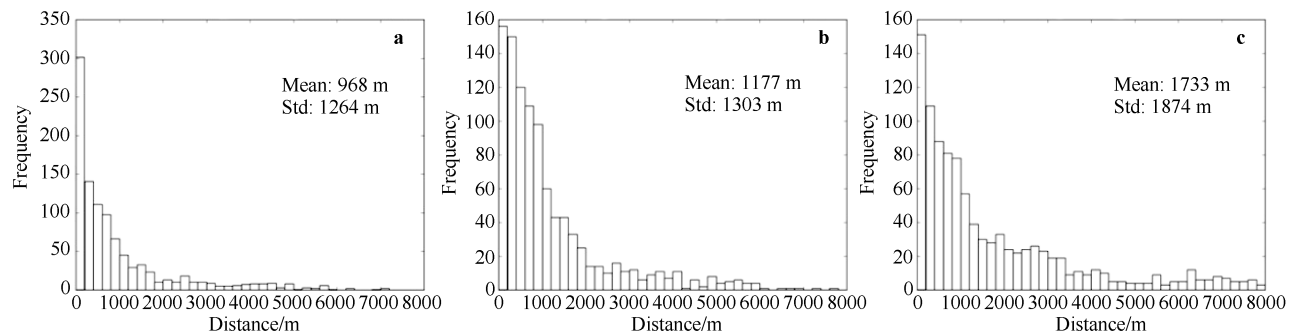
Figure 5　Histograms of distance between MEaSUREs and Sentinel-1 GLs (**a**), synthesized and Sentinel-1 GLs (**b**), MOA and Sentinel-1 GLs (**c**).

Table 2　Sentinel-1 GL error assessment

Matching degree \ Buffers \ GL products	1 km buffer	2 km buffer	3 km buffer
MEaSUREs	72.42%	86.30%	92.24%
Synthesized	69.32%	85.75%	90.35%
MOA	52.06%	68.26%	79.32%

4.3 GL change detection

Figure 6a illustrates the distance between Sentinel-1 and MEaSUREs GLs. This is shown in blue for < 1 km, in green between 1 and 2 km, in yellow between 2 and 3 km, and in red for > 3 km. Comparing our results with the MEaSUREs GL, three regions (shown by black boxes in Figure 6a) have the largest differences.
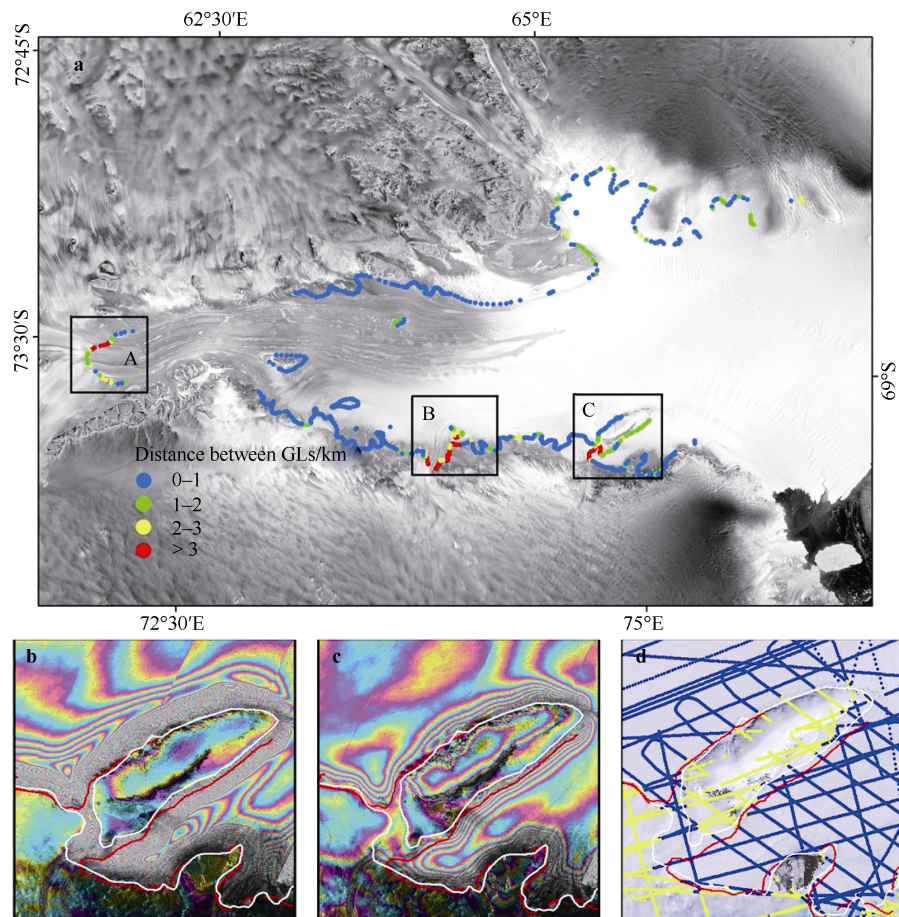
Figure 6 Differences between Sentinel-1 and MEaSUREs GLs (**a**). DDSI-2 of region C with tide height difference = 1.03 m (**b**). DDSI-9 of region C with tide height difference = 0.02 m (**c**). HE ice thickness anomaly results for region C (**d**) (ice thickness anomaly < −209.45 m shown in yellow, and > −209.45 m in blue).

Figure 4d and region A in Figure 6a show an inset of the southernmost GL on the AIS, at the confluence zone of the Lambert, Mellor, and Fisher Glaciers. The ice speed was as high as 800 m·a^{-1} in this area. The GL could only be detected using short temporal baseline SAR pairs. Clear tidal signals were observed in the DDSI with 6-day repeat cycle, and the southernmost GL was around 73.2°S. Our results are consistent with previous RES results. Fricker et al. (2002) used the hydrostatic method to estimate the hydrostatic point (*H*), and the most southerly determined position of *H* from their hydrostatic calculations was roughly 73.2°S. Rignot (2001) used an ERS-1/2 tandem InSAR interferogram (1-d repeat cycle) acquired in 1996 to map the GL in this area. This is shown in Figure 7, in which the HE ice thickness anomaly results are shown as a yellow dot if < −209.45 m, indicating that the ice is grounded. The Sentinel-1 GL approximately matches both the MEaSUREs GL and HE results, and the difference would be from a difference in tide height. The GL in the southernmost part of the AIS shows no obvious evidence of retreat over the last 20 years. However, in West Antarctica, the GL in the Amundsen Sea region is retreating rapidly (Scheuchl et al., 2016). Ice shelf bottom melt can directly cause retreat of the GL (Schoof, 2007). The greatest basal melt always comes from medium to small ice shelves, but not from the largest ones, such as the Ross and Ronne ice shelves and the AIS. The mean basal–mass loss rate is relatively small for the AIS (0.8 m·a^{-1}), and > 7 m·a^{-1} in the Amundsen Sea (Depoorter et al., 2013a).
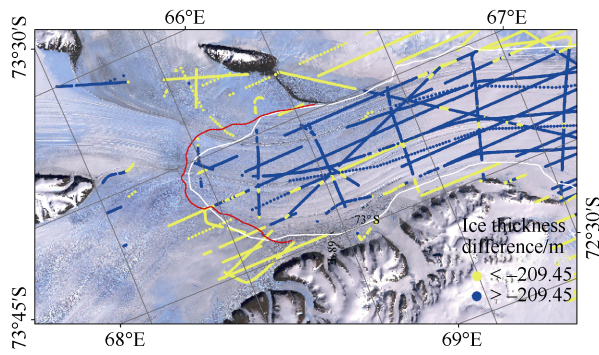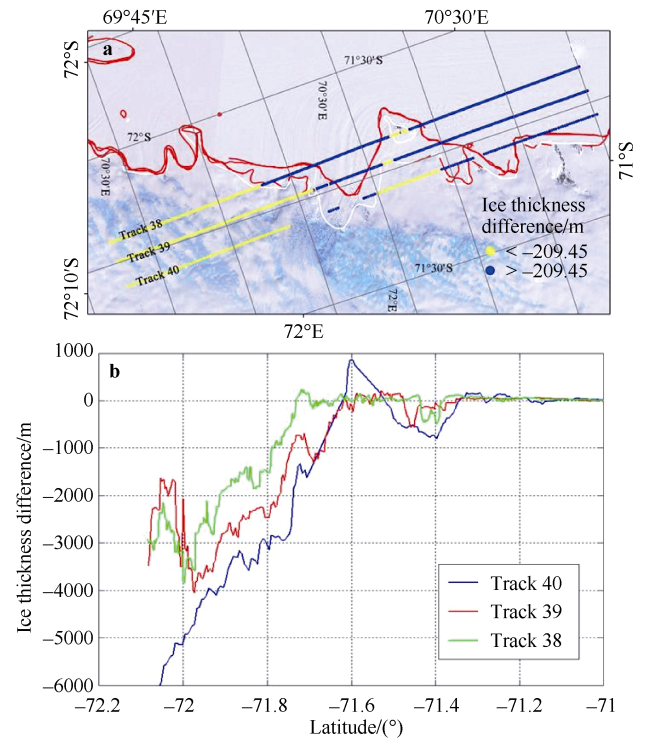
Figure 7   HE ice thickness anomaly results for the southernmost GL of AIS (blue and yellow dots). White GL is result from Sentinel-1 and red GL from MEaSUREs.

Figure 4e and region B in Figure 6a show the Kronshtadtskiy Glacier. That glacier flows northwestward and enters the AIS ~8 km southeast of Pickering Nunatak. The ice speed is 600 m·a^{-1} at the center of the glacier and 270 m·a^{-1} along the broad side. This is the fastest glacier entering the AIS from the east. As shown in Figure 4e, there are maximum differences of 8.7 km between the Sentinel-1 and MEaSUREs GLs. These differences suggest that either the GL has retreated over the past 16 years or that the change of tides greatly affected GL mapping. To gain further insight into this area, HE ice thickness anomaly results of Tracks 38, 39, and 40 are shown (Figure 8a). Ice thickness anomalies < –209.45 m are shown by yellow dots, indicating that the ice is grounded. Figure 8b portrays ice thickness difference profiles along the three tracks. The HE results show good agreement with our results. Considering that the HE results represent the GL before 2000, the conclusion that the change of tides affected GL mapping is most likely.

Figure 4f and region C in Figure 6a show an inset of Gillock Island on the eastern side of the AIS. A previous GL showed that the inner SAR fringe is not close, and either the channel between the island and ice sheet is narrow or the island is joined to the mainland at low tide (Fricker et al., 2009). We used five Sentinel-1 acquisitions to create two DDSIs for this area, and tide model CATS2008a was used to predict tide height. As shown in Figure 6, the inner SAR fringe is close in Figure 6b but not in Figure 6c. The difference of tide height predicted by CATS2008a is 1.04 and 0.02 m in Figures 6b and 6c, respectively. The HE ice thickness anomaly result is shown in Figure 6d, indicating that the channel between the island and ice shelf is near HE. The island is separated from the mainland, and the GL between the island and mainland can be easily detected by DDInSAR at high tide.

5   Conclusions

Mapping the GL on the AIS using DDInSAR is challenging because of substantial signal decorrelation over long

Figure 8   HE ice thickness anomaly results for Kronshtadtskiy Glacier. White GL is result from Sentinel-1 and red GL from MEaSUREs (**a**). Ice thickness difference profiles of Tracks 38, 39, and 40 (**b**).

periods, surface melt, and strong accumulation. The 6-day repeat cycle Sentinel-1 constellation data show a remarkable ability to map the GL in fast-moving portions of the glaciers. Using Sentinel-1 data, we mapped a relatively complete InSAR-based GL of the AIS. The RES data demonstrate that the Sentinel-1 GL outperformed existing Antarctic GL products in both accuracy and range.

In specific locations, Sentinel-1 GL is somewhat different from previous maps, and tide changes greatly affected the distribution of interferometric dense fringes. With the new GL, we detected new ice rises on the northwestern AIS, enhancing our understanding of the ice-flow pattern in that area. By comparing InSAR data acquired 20 years earlier, we found no major retreat of the GL, especially the southernmost GL. Further study is needed to evaluate the difference between steady state conditions of the AIS and major changes in West Antarctica, particularly around the Amundsen Sea. Furthermore, with the Sentinel-1 data, ice surface velocity can be mapped to estimate ice flux changes on the AIS, which can contribute to mass balance research of East Antarctica.

References

Allison I, Hyland G. 2010. Amery Ice Shelf compiled and merged ice thickness datasets. Australian Antarctic Data Centre - CAASM Metadata. https://data.aad.gov.au/metadata/records/AIS_thickness_bottom

Bamber J L, Gomez-Dans J L, Griggs J A. 2008. A new 1 km digital elevation model of the Antarctic derived from combined satellite radar and laser data-Part 1: Data and methods. Cryosphere, 3(1): 101–111

Bindschadler R, Choi H, Wichlacz A, et al. 2011. Getting around Antarctica: new high-resolution mappings of the grounded and freely-floating boundaries of the Antarctic ice sheet created for the International Polar Year. Cryosphere, 5(3): 569–588, doi: 10.5194/tc-5-569-2011

Brunt K M, Fricker H A, Padman L, et al. 2010. Mapping the grounding zone of the Ross Ice Shelf, Antarctica, using ICESat laser altimetry. Ann Glaciol, 51(55): 71–79, doi: 10.3189/172756410791392790

Chuter S J, Bamber J L. 2015. Antarctic ice shelf thickness from CryoSat-2 radar altimetry. Geophys Res Lett, 42(24): 10721–10729, doi: 10.1002/2015GL066515

De Zan F, Prats-Iraola P, Scheiber R, et al. 2014. Interferometry with TOPS: coregistration and azimuth shifts//Proceedings of the 10th European conference on synthetic aperture radar. Berlin Germany: IEEE, 2014: 1–4

Depoorter M A, Bamber J L, Griggs J A, et al. 2013a. Corrigendum: Calving fluxes and basal melt rates of Antarctic ice shelves. Nature, 502(7472): 580, doi: 10.1038/nature12737

Depoorter M A, Bamber J L, Griggs J A, et al. 2013b. Calving fluxes and basal melt rates of Antarctic ice shelves. Nature, 502(7472): 89–92, doi: 10.1038/nature12567

Förste C, Bruinsma S, Flechtner F, et al. 2013. EIGEN-6C2—A new combined global gravity field model including GOCE data up to degree and order 1949 of GFZ Potsdam and GRGS Toulouse//EGU general assembly conference abstracts, volume 15. Vienna: General Assembly European Geosciences Union, 620–622

Fricker H A, Hyland G, Coleman R, et al. 2000. Digital elevation models for the Lambert Glacier–Amery Ice Shelf system, East Antarctica, from ERS-1 satellite radar altimetry. J Glaciol, 46(155): 553–560, doi: 10.3189/172756500781832639

Fricker H A, Popov S, Allison I, et al. 2001. Distribution of marine ice beneath the amery ice shelf. Geophys Res Lett, 28(11): 2241–2244

Fricker H A, Allison I, Craven M, et al. 2002. Redefinition of the Amery Ice Shelf, East Antarctica, grounding zone. J Geophys Res, 107(B5): ECV 1-1–ECV 1-9

Fricker H A, Coleman R, Padman L, et al. 2009. Mapping the grounding zone of the Amery ice shelf, East Antarctica using InSAR, MODIS and ICESat. Antarct Sci, 21(5): 515–532, doi: 10.1017/S095410200-

999023X

Griggs J A, Bamber J L. 2011. Antarctic ice-shelf thickness from satellite radar altimetry. J Glaciol, 57(203): 485–498, doi: 10.3189/0022143-11796905659

Hall J K. 2006. GEBCO centennial special issue-charting the secret world of the ocean floor: The GEBCO Project 1903–2003. Mar Geophys Res, 27(1): 1–5, doi: 10.1007/s11001-006-8181-4

Lenaerts J T M, Brown J, van den Broeke M R, et al. 2014. High variability of climate and surface mass balance induced by Antarctic ice rises. J Glaciol, 60(224): 1101–1110, doi: 10.3189/2014JoG14J040

Ligtenberg S R M, Kuipers Munneke P, van den Broeke M R. 2014. Present and future variations in Antarctic firn air content. Cryosphere, 8(5): 1711–1723, doi: 10.5194/tc-8-1711-2014

Prats-Iraola P, Nannini M, Scheiber R, et al. 2015. Investigations with the Sentinel-1 interferometric wide swath mode//ESA FRINGE workshop. Proceedings of ESA FRINGE workshop. Frascati: ESA FRINGE workshop

Rignot E. 1998. Radar interferometry detection of hinge-line migration on Rutford Ice Stream and Carlson Inlet, Antarctica. Ann Glaciol, 27: 25–32

Rignot E. 2001. Mass balance of East Antarctic glaciers and ice shelves from satellite data. Ann Glaciol, 34: 217–227

Rignot E, Thomas R H. 2002. Mass balance of polar ice sheets. Science, 297(5586): 1502–1506, doi: 10.1126/science.1073888

Rignot E, Mouginot J, Scheuchl B. 2011. Antarctic grounding line mapping from differential satellite radar interferometry. Geophys Res Lett, 38(10): L10504, doi: 10.1029/2011GL047109

Rignot E, Jacobs S, Mouginot J, et al. 2013. Ice-shelf melting around Antarctica. Science, 341(6143): 266–270, doi: 10.1126/science.1235798

Scambos T A, Haran T M, Fahnestock M A, et al. 2007. MODIS-based Mosaic of Antarctica (MOA) data sets: Continent-wide surface morphology and snow grain size. Remote Sens Environ, 111(2–3): 242–257

Scheiber R, Moreira A. 2000. Coregistration of interferometric SAR images using spectral diversity. IEEE Trans Geosci Remote Sens, 38(5): 2179–2191, doi: 10.1109/36.868876

Scheuchl B, Mouginot J, Rignot E, et al. 2016. Grounding line retreat of Pope, Smith, and Kohler Glaciers, West Antarctica, measured with Sentinel-1a radar interferometry data. Geophys Res Lett, 43(16): 8572–8579, doi: 10.1002/2016GL069287

Schoof C. 2007. Ice sheet grounding line dynamics: steady states, stability, and hysteresis. J Geophys Res, 112(F3): F03S28, doi: 10.1029/2006JF000664

Torres R, Snoeij P, Geudtner D, et al. 2012. GMES sentinel-1 mission. Remote Sens Environ, 120: 9–24, doi: 10.1016/j.rse.2011.05.028

Wang Q H, Ning J S, Ren J W, et al. 2002. Re-definition and validation of the grounding line of Amery Ice Shelf, East Antarctica. Geomat Inf. Sci Wuhan Univ, 27(6): 591–597 (in Chinese)

Weertman J. 1974. Stability of the junction of an ice sheet and an ice shelf. J Glaciol, 13(67): 3–11

Wegmüller U, Werner C, Strozzi T, et al. 2015. Sentinel-1 IWS mode support in the GAMMA software//Proceedings of the 5th Asia-Pacific conference on synthetic aperture radar (APSAR). Singapore: IEEE, 2015: 431–436, doi: 10.1109/APSAR.2015.7306242

Wen J H, Wang Y F, Wang W L, et al. 2010. Basal melting and freezing

under the Amery Ice Shelf, East Antarctica. J Glaciol, 56(195): 81–90, doi: 10.3189/002214310791190820

Werner C L, Wegmüller U, Strozzi T, et al. 2001. Gamma SAR and interferometric processing software//Sawaya-Lacoste H. ERS-ENVISAT symposium. Gothenburg: European Space Agency Publications Division

Xie H, Chen L, Liu S, et al. 2016. A least-squares adjusted grounding line

for the Amery Ice Shelf using ICESat and Landsat 8 OLI data. IEEE J Sel Top Appl Earth Obs Remote Sens, 9(11): 5113–5122, doi: 10.1109/JSTARS.2016.2614758

Yagüe-Martínez N, Prats-Iraola P, González F R, et al. 2016. Interferometric processing of sentinel-1 TOPS Data. IEEE Trans Geosci Remote Sens, 54(4): 2220–2234, doi: 10.1109/TGRS.2015.2497902